Journal of Magnetic Resonance 201 (2009) 239–249

Contents lists available at ScienceDirect

Journal of Magnetic Resonance

journal homepage: www.elsevier.com/locate/jmr

A single-chip array of NMR receivers

Jens Anders *, Giuseppe Chiaramonte, Paul SanGiorgio, Giovanni Boero

Ecole Polytechnique Fédérale de Lausanne (EPFL), CH-1015 Lausanne, Switzerland

ARTICLE INFO

Article history:
Received 22 June 2009
Revised 17 September 2009
Available online 2 October 2009

Keywords:
Micro-MRI
CMOS
NMR
Array

ABSTRACT

We present the first single-chip array of integrated NMR receivers for parallel spectroscopy and imaging. The array, optimized for operation at 300 MHz, is composed of eight separate channels, with each channel consisting of a detection coil, a tuning capacitor, a low noise amplifier and a 50 Ω buffer. As all the integrated electronics are placed underneath the reception coils, the array is densely packed. Each single-channel reception coil has a diameter of 500 μm, resulting in a total active area of 1 mm by 2 mm for the array. The ^{1}H time-domain spin sensitivity of a single channel is approximately 1×10^{15} spins/$\sqrt{\text{Hz}}$.

1. Introduction

Standard nuclear magnetic resonance (NMR) systems use high-quality factor reception coils and low-noise Gallium-Arsenide electronics in their radio-frequency (RF) frontend. Recently, there has been considerable effort to combine up to 128 of these discrete-component receivers into large arrays [1–6]. For imaging, an array of receivers can be used to increase the field-of-view while maintaining the spatial resolution of the component receivers. Alternatively, one can apply the idea of parallel imaging [7] by positioning the different receivers to reduce the effective number of measurement points in the *k*-space. Moreover, such an array can also be used for parallel spectroscopy, drastically increasing the possible throughput of NMR-spectrometers [8–16]. Unfortunately, the conventional approach of combining standard, discrete reception channels into large arrays also poses several drawbacks. Not only are such systems rather expensive but they also become very bulky if large array sizes are desired. The latter drawback is particularly important for micro-imaging and spectroscopy where the coil sizes are adapted to the sample volume to achieve optimum spin sensitivity [14,17–20]. Here, the size difference between reception coil and discrete electronics renders the design of a large, yet spatially compact array virtually impossible. In this paper, we propose the use of an inexpensive standard complementary metal-oxide-semiconductor (CMOS) technology to build large receiver arrays with good performance. Recently, there have been other attempts that exploit integrated electronics for NMR applications: Reception coil and receiver electronics were placed on the same IC to form a single receiver for NMR magnetometry [21]; external coils were combined with CMOS chips to form hybrid systems for magnetometry [22] and NMR-spectroscopy [23]; and, chips with a high level of integration were combined with external coils to perform very specific tasks such as spectral scanning MRI [24] or to form more complex systems for biomolecular sensing [25]. Our attempt is the first array of receivers with integrated electronics and reception coils co-integrated on the same IC. Co-integrating the electronics and the reception coil on the same chip allows us to adapt the coil sizes for very small samples and to have spatially compact arrays with a large number of reception channels.

The paper is organized as follows. In Section 2 we first describe a single-channel integrated receiver component-by-component and then explain how the single channels are combined into an array; a brief description of the external electronics is also included. In Section 3 we show measurements of the receiver array and compare them to simulations. The paper ends with some concluding remarks and a brief outlook on future work.

2. Receiver electronics

The receiver electronics consist of a single silicon chip, described in Section 2.1, and a printed circuit board (PCB), described in Section 2.3, providing the interface electronics between the chip and the data acquisition system.

2.1. Single-chip integrated electronics

The single-chip array is implemented in a 0.35 μm CMOS technology from Austriamicrosystems (Unterpraemstetten, Austria).

* Corresponding author. Address: Ecole Polytechnique Fédérale de Lausanne (EPFL), STI LMIS3, EPFL STI IMT LMIS3, BM 3108 Station 17, CH-1015 Lausanne, Switzerland. Fax: +41 216936670.
E-mail address: jens.anders@epfl.ch (J. Anders).

1090-7807/$ - see front matter © 2009 Elsevier Inc. All rights reserved.
doi:10.1016/j.jmr.2009.09.019

2.1.1. Detection coil and tuning capacitor

The NMR signal is detected using a square on-chip coil whose geometry is optimized for a maximum signal-to-noise ratio (SNR) at the operating frequency of 300 MHz. The coil is made of aluminum with a nominal thickness of 2.7 μm and a corresponding sheet resistance of 10 mΩ/□. The geometrical optimization was performed for a fixed outer diameter of 500 μm to achieve the largest SNR for a sample with a volume of about $(500\ \mu m)^3$ using reciprocity principle [26] based calculations for the estimation of the signal and assuming the dominant sources of noise to be the coil resistance and the input referred noise of the low-noise amplifier (LNA). The optimized coil has an inductance of about 17 nH and a resistance of 4 Ω at 300 MHz, resulting in an unloaded Q-factor of roughly 8 at 300 MHz. The coil resistance corresponds to a voltage noise density of $0.3\ nV/\sqrt{Hz}$. The coil dimensions and the equivalent electrical circuit are shown in Fig. 1. The equivalent circuit was determined using electromagnetic simulations with the Virtuoso Passive Component Modeler (VPCM) (Cadence). To obtain some noise-free preamplification, a fixed polysilicon–silicon oxide–polysilicon capacitor is integrated in parallel with the reception coil. The value of the capacitor is chosen for an optimal noise performance. After a first numerical optimization using a simplified circuit model in MATLAB (The MathWorks), the final capacitance value of $C \cong 15$ pF was found by SpectreRF (Cadence) simulations. Therefore, although the theoretically optimal choice for the noise-matching capacitor resonates with the reception inductor at a frequency slightly lower than $\omega_0 = 300$ MHz, given process variations, it does not lead to a significant performance degradation to choose it according to $C = 1/(\omega_0^2 L)$.

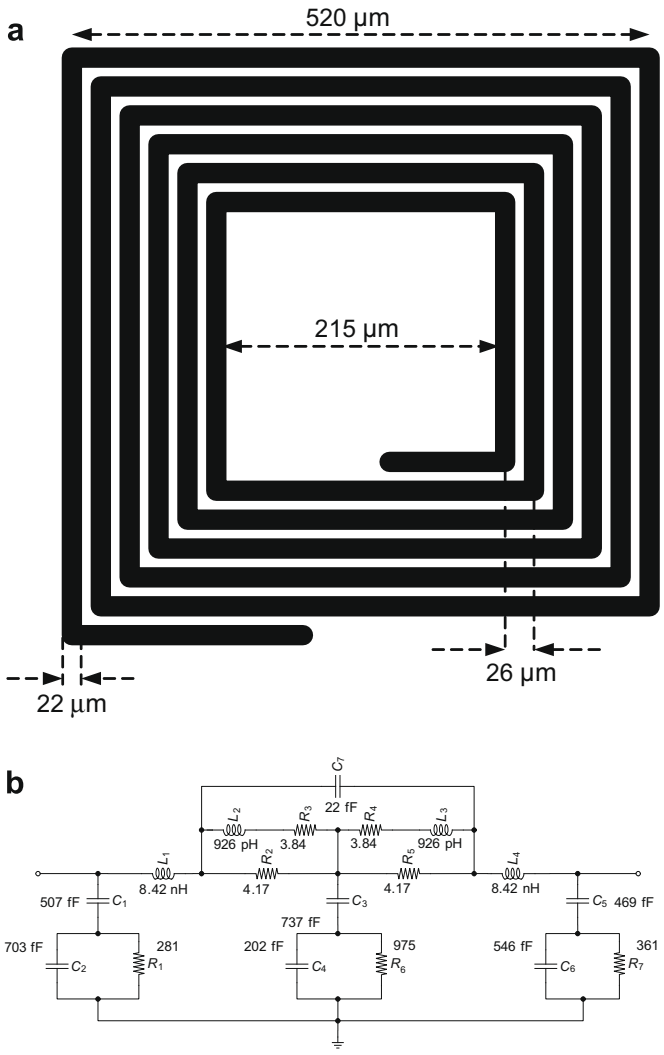

Fig. 1. Details of the detection coil. (a) Coil geometry. (b) Coil equivalent circuit around 300 MHz as determined using the VPCM tool.

2.1.2. Low noise amplifier

A schematic of the integrated LNA is shown in Fig. 2. The differential voltage amplifier topology reduces any common-mode interferences from the supply lines and thereby reduces the electrical crosstalk between different channels. A differential-to-single-ended conversion is performed at the output of the LNA to simplify the connection to the electronics of standard NMR/MRI-systems. To reduce the power consumption while still providing a low input-referred noise voltage level, a current-reuse technique is exploited in the input differential pair by stacking an NMOS and a PMOS pair in parallel. This technique allows us to achieve an input referred noise level close to the noise level generated by the intrinsic resistance of the reception coil, and therefore to avoid significant degradation of the receiver performance while keeping the overall power consumption low enough to prevent self-heating, even when many such receivers are used to form large arrays. Despite those precautions, the 80 mA drawn from the 3.3 V supply heat up the chip to about 70 °C if it is mounted on an ordinary FR4 printed circuit board (PCB) and no further means are applied to improve the heat transfer from the chip to the PCB. However, gluing the chip to a ceramic substrate using a thermal conductive glue and a thermal conductive adhesive to protect the bond wires reduces the working chip temperature to approximately 40 °C.

To avoid further degradation of the overall noise performance by the integrated electronics, the total gate resistance of the input pairs has to be significantly smaller than the coil resistance multiplied by the preamplification of the LC-circuit. This is achieved by careful layout of the input differential pairs. These are laid out as common centroids where each half transistor is first divided in three diffusion areas and then fingered.

Transistor M_{p7} serves the purpose of both reducing the output impedance of the first stage – which extends the bandwidth to the required 300 MHz – and providing a proper bias voltage. A more detailed description of the circuitry and the design procedure applied can be found in [27].

2.1.3. Output buffer

Similar to the case of the LNA, the tight area constraints prohibit the use of reactive elements for the output matching. Therefore, to achieve an output impedance of 50 Ω, two source followers have to be used to obtain the low output impedance over the desired bandwidth of 300 MHz because reducing the impedance in a single very large step would lead to undesired peaking in the frequency response [28]. By choosing the single impedance steps optimally, one can maximize the bandwidth of the buffer [28]. The optimal choice lead to a first impedance step from 1.5 kΩ to about 300 Ω and the second step yields the desired 50 Ω output impedance. The corresponding schematic is shown in Fig. 2.

2.2. Receiver array

A block-diagram of the array is shown in Fig. 4. It is composed of eight of the single-channels described in Section 2.1 which are used as standard cells and placed as shown in Fig. 5b. This configuration minimizes the number of supply connections and maximizes the symmetry of the array by proper abutting and mirroring of the standard cells. Due to the tight area constraints imposed by making a densely packed array, no special means were taken to isolate the channels electrically, that is, no guard rings are placed around the single channels. As it will be shown in Section

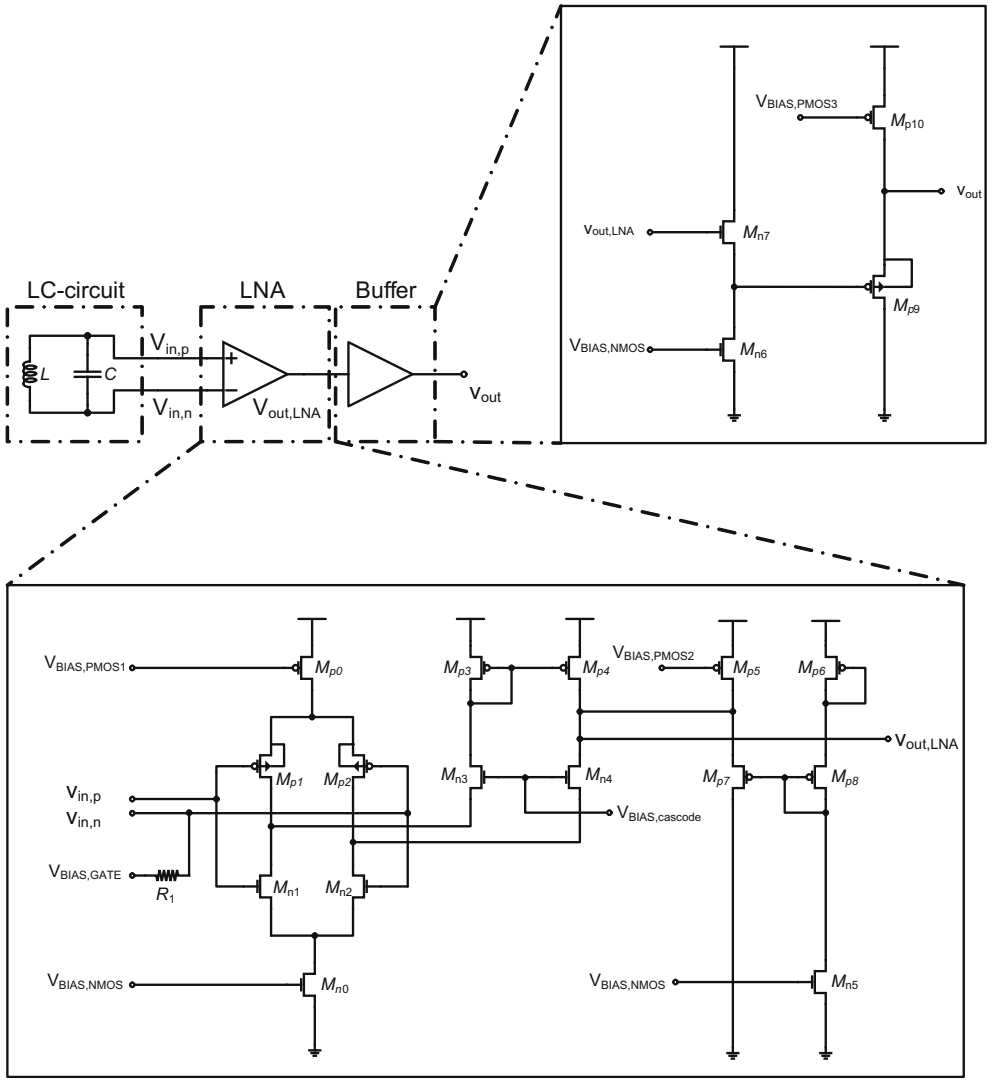

Fig. 2. Block-diagram and detail schematics of a single reception channel. The on-chip circuitry to generate all bias voltages from a single power supply is shown in Fig. 3.

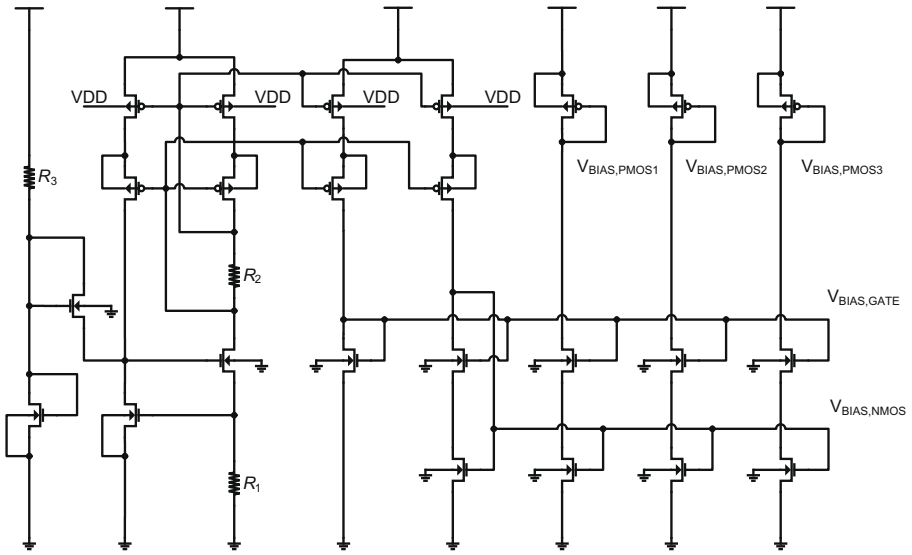

Fig. 3. Schematic of the on-chip bias voltage generation.

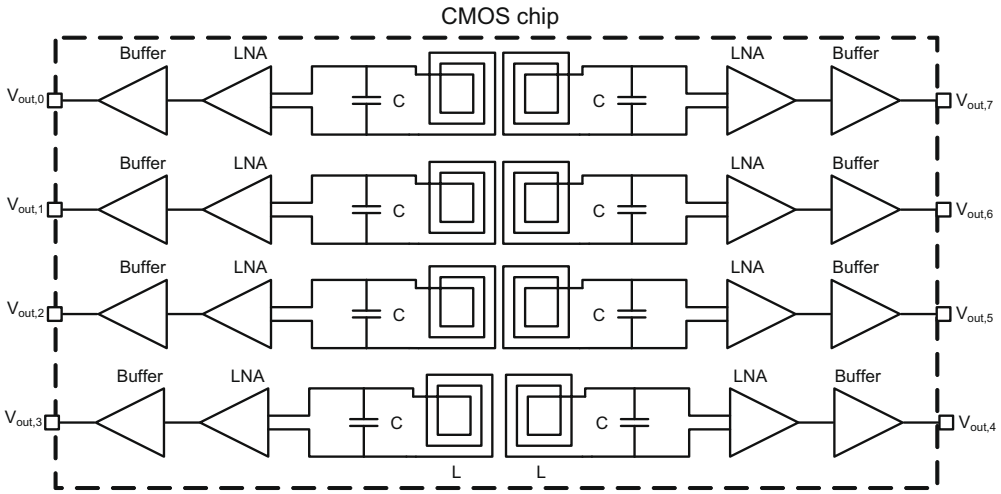

Fig. 4. Block-diagram of the integrated receiver.

3.2 the lack of guard rings does not degrade the receiver performance.

2.3. Discrete electronics

The RF-NMR signals coming from the CMOS-chip are further amplified and downconverted to low-frequencies by discrete electronics on an 8-channel custom-made printed circuit board (PCB). Each channel is composed of an additional RF amplification stage, a downconversion mixer and a low-frequency combined amplification and filtering stage. The architecture is illustrated as part of Fig. 9. The RF amplification chain is made up of two monolithic amplifiers (Gali-39+ Minicircuits) each one with a typical power gain of 23 dB and a noise figure of 2 dB at 300 MHz. A 2 dB matched attenuator is placed between the amplifiers to prevent oscillations and to improve the impedance matching between the amplifiers. The amplified RF signal is then fed into a double-balanced mixer (AD831 Analog Devices) performing the downconversion to low frequencies. The mixer has a conversion gain of 0 dB and an integrated low-frequency amplifier with settable gain, which was fixed to 20 dB in our configuration using an external resistive network. The sum-frequency component is suppressed by a one-pole low-pass filter consisting of two resistors integrated in the mixer and external capacitors. The 0 dBm local oscillator signal is provided by a signal generator (MG3633A Anritsu).

The gain in the IF stage can be selected between 20 and 66 dB using jumpers. An additional jumper gives the possibility to select one of two third-order unity-gain anti-aliasing filters (with cutoff frequencies 30 and 120 kHz, respectively). Both filters are designed as a Sallen-Key cell followed by a simple one-pole low-pass filter. The IF signals at the output of the external 8-channel electronics are simultaneously digitized and processed by a Labview (National Instruments) program.

The excitation coil used for all experiments is a single-turn, planar coil on a PCB with an inner diameter of 4.5 mm. The 90°-pulse length of the coil is about 10 μs for an excitation power of 40 dBm. A photograph of the excitation coil is shown in Fig. 8 as part of the probe.

3. Simulations and measurements

3.1. Circuit level simulations

The performance of the integrated electronics was simulated using the circuit simulator SpectreRF. Input referred noise and gain were evaluated using a periodic noise (PNoise) and periodic AC (PAC) analysis, respectively, to achieve the highest accuracy possible. The simulation results obtained from an extracted view simulations containing all parasitic resistances and capacitances of the final layout are shown in Fig. 6.

3.2. Receiver characterization using NMR-spectroscopy

Reception coil and integrated electronics are fabricated as a single IC. To avoid capacitive loading of the coil, there are no test pads at the input of the LNA that would allow a separate testing of the LNA behavior. Therefore, no direct electrical testing of the LNA performance, i.e. gain and noise, can be performed and two NMR-based methods are used to characterize the integrated receiver.

In the first method, the induced voltage in the receiver coil is calculated from the net nuclear magnetization of the sample M_0, the sample volume V_0, the coil geometry and the magnetic field generated by a 1-ampere current in the coil, B_u. Knowing the induced voltage, one can estimate the gain by simply measuring the initial FID amplitude at the chip output after a 90°-pulse. Once the gain is measured one can calculate the input referred noise by dividing the measured output voltage noise spectral density by the gain.

The second method uses the 90°-pulse length to estimate the B_1-field for a certain output power-level of the power amplifier connected to the excitation coil according to $\theta = \gamma B_1 \tau$, where γ is the gyromagnetic ratio and τ is the measured pulse length. Knowing the B_1-field for the power-level required to create the 90°-pulse, one can reduce the power until the chip works in the linear region and linearly amplifies the induced voltage at its input. Once the chip works in the linear region, one can calculate the B_1-field corresponding to the reduced output power-level of the power amplifier. Afterwards, one can calculate the induced voltage, knowing the chip-coil geometry and assuming a uniform B_1-field over the coil surface. Once the induced voltage is calculated the remainder of this method is identical to the first one. The two methods give an estimation of the gain which differ by less than 15%. The absolute accuracy of the two methods can be estimated in the following way: For the first method, the only uncertainty comes from the geometry of the sample. To quantify this error, we assumed tolerances on the sample size and calculated the resulting gain for the extreme cases. The resulting error was about 3 dB. For the second method, the estimate of the effective B_1-field should be very precise because it is based on measuring the 90°-excitation pulse. Therefore, the only possible source of error in this method is the inhomogeneity of the B_1-field over the reception coil.

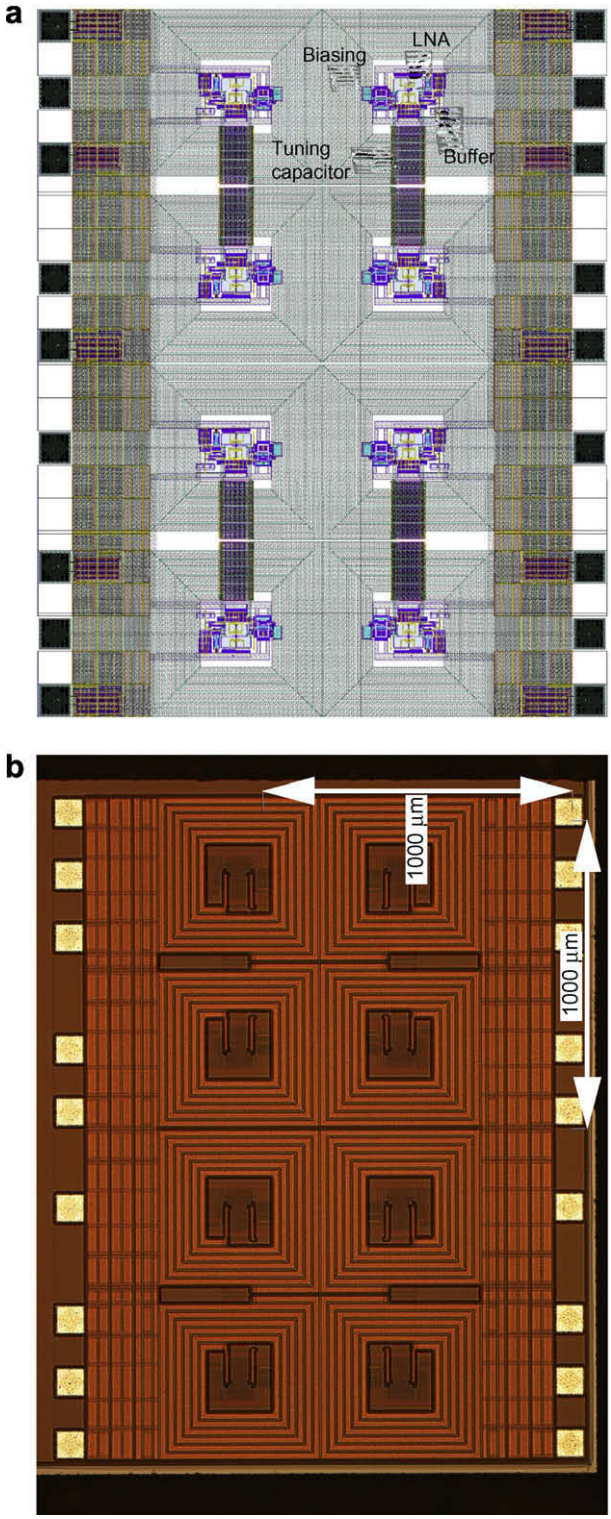

Fig. 5. Single silicon chip array of NMR-receivers: (a) layout; (b) microphotograph.

Since the diameter of the excitation coil is about 2.5 times the diameter of the reception array, the field on the edges of the array is about 7% larger than the field in the center and the resulting error is a below a factor of $\sqrt{2}$. Thus, the absolute error for both method is below a factor of 3 dB.

As a first test, the gain variation from channel to channel was examined. To this end, the excitation coil was placed on top of the receiver chip to excite all channels homogeneously. Then, the

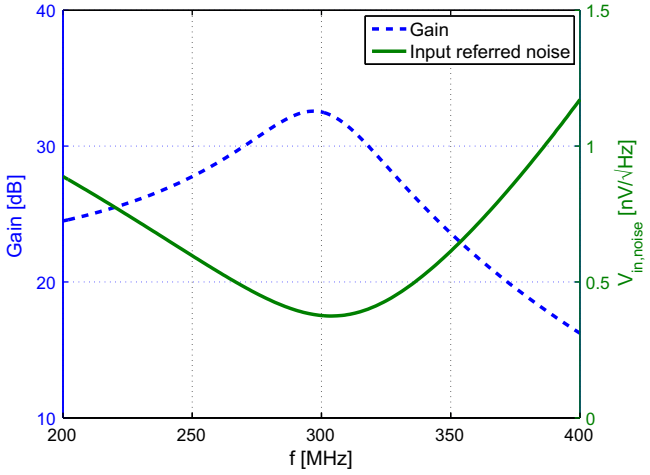

Fig. 6. Noise and gain simulation.

output signal of each channel on the PCB was recorded. It was found that the gain and noise variations from channel to channel are less than 12%, including the variations from the external electronics. Next, the receiver performance was evaluated using the two methods described above. Gain and noise were evaluated channel-by-channel and compared with simulations. The results of these experiments are displayed in Table 1.

3.3. Measurements

The setup used to perform the NMR experiments is shown in Fig. 7. In order to evaluate the NMR performance of the integrated receiver, NMR-spectroscopy experiments using both solid and liquid samples have been performed. For the liquid samples, two capillaries with different dimensions were used. The first one has an inner diameter of 180 µm and an outer diameter of 350 µm resulting in a sample volume of 12 nl over a 500 µm channel. The second capillary has an inner diameter of 375 µm and an outer diameter of 530 µm resulting in a sample volume of 55 nl over a 500 µm channel. In a first spectroscopy experiment, a 1 mm × 2 mm × 0.5 mm solid sample of polydimethylsiloxane (PDMS) (DOW CORNING Sylgard 184) covering the whole receiver array was analyzed. This sample has an approximate ^{1}H spin density of $N = 4 \times 10^{28}$ spins/m^3 and a T_2-time of 2 ms at 7 T (300 MHz) and 300 K. The geometry is illustrated in Fig. 9a. Following a 90°-excitation pulse the FID was recorded for each channel. The measured time-domain signals are shown in Fig. 10a and the real parts of the corresponding FFT are displayed in Fig. 10b, respectively. The full width half maximum (FWHM) linewidths are [160, 195, 190, 160, 240, 165, 185 and 195 Hz] for channels 0 through 7. Next, a liquid sample, isopropanol, was mounted (55 nl capillary, length: 4 cm) on the left four channels of the array to evaluate the achievable line-width of the system without room temperature shimming. The capillary length was chosen such that it greatly exceeded the chip's active region and thus minimized linewidth broadening due to the sample geometry; the setup is illustrated in Fig. 9b. The extension of the capillary into the less

Table 1
Gain and input referred noise of the integrated RF-receiver at 300 MHz: comparison between measured and simulated (including process variations) values.

	Measured	Simulated
Voltage gain (dB)	28 ± 3	30 ± 3
$v_{in,\ noise}$ (nV/$\sqrt{Hz}$)	0.6 ± 0.2	0.4 ± 0.03

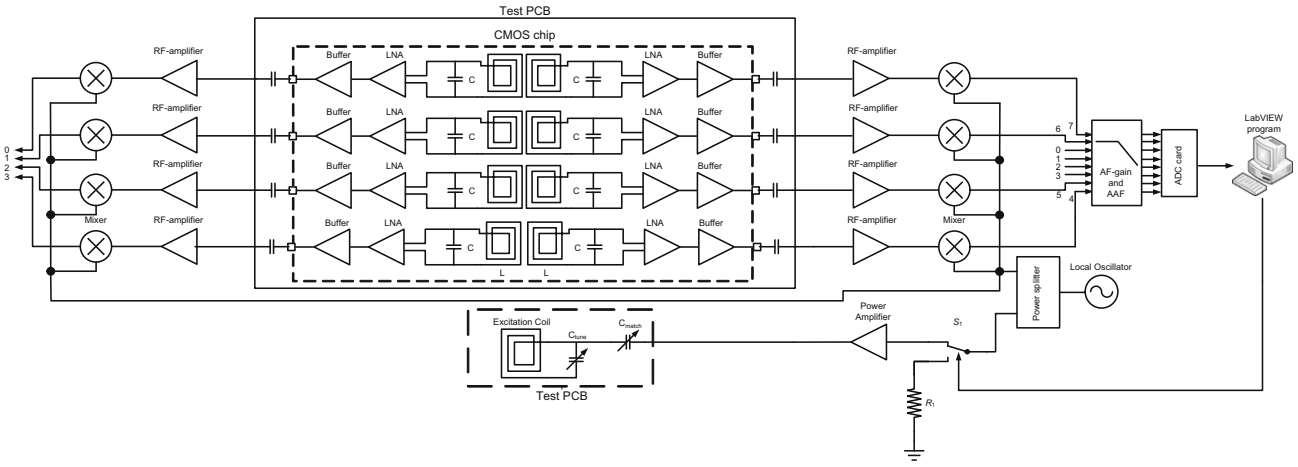

Fig. 7. Test setup used to evaluate the chip performance.

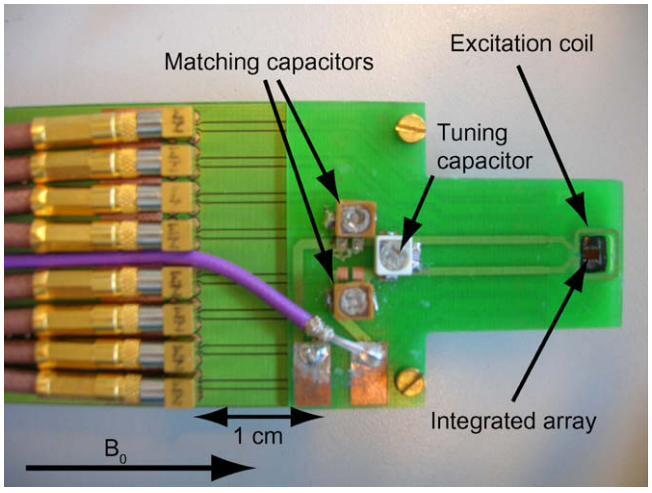

Fig. 8. PCB containing the integrated array of NMR-receivers and the excitation coil with its corresponding tuning and matching network.

homogeneous region of the magnetic field is beneficial because we work in a situation where the main limitation for spectral resolution is sample induced line shape broadening in a situation where spectral resolution would be limited by the homogeneity of the magnetic field, the opposite would be true. The corresponding FIDs and spectra for all eight channels are displayed in Fig. 11a and b, respectively. The peak FID amplitudes of the channels covered by the sample are all within ±30% and the FWHM linewidths are [40, 20, 20 and 30 Hz] for channels 0 through 3.

3.3.1. Spin sensitivity

The sensitivity of an NMR detector is usually given in terms of "concentration sensitivity" and "spin sensitivity". It is the spin sensitivity which is significantly improved through the use of miniaturized inductive detectors [29]. Let us assume that the time-domain signal after the end of the RF-excitation can be written as

$$s(t) = \sum_i s_{0,i} \cos\left(\omega_{0,i} t\right) \exp\left(-t/T_2^\star\right) + n(t), \tag{1}$$

where $s_{0,i}$ and $\omega_{0,i}$ are the amplitude and the frequency of the different spectral lines and $n(t)$ represents the noise. The frequency-domain SNR can be defined as

$$\mathrm{SNR}_{f,i} \equiv \frac{S_{\omega_{0,i}}}{2N_{rms}} = \frac{s_{0,i} T_2^\star \left(1 - \exp\left(-T_{ACQ}/T_2^\star\right)\right)}{4 n_{rms} \sqrt{T_{ACQ}}/\sqrt{2B}}, \tag{2}$$

where $S_{\omega_{0,i}}$ is the amplitude of the spectral line at the angular frequency $\omega_{0,i}$ in the real part of the FFT, N_{rms} is the rms value of the noise fluctuations in the real part of the FFT at the angular frequency $\omega_{0,i}$, T_{ACQ} is the acquisition time, n_{rms} is the rms value of the white noise process $n(t)$ and B is the equivalent noise bandwidth of the receiver electronics.

For optimum SNR in the frequency-domain, the time-domain signal is usually multiplied by the "matched filter" function $\exp(-t/T_2^\star)$. Assuming an acquisition time much longer than $T_2^\star$, i.e. $T_{ACQ} \gg T_2^\star$, we obtain $S_{\omega_{0,i}} \approx (1/4) s_{0,i} T_2^\star$ and $N_{rms} \approx (1/2)(n_{rms}/\sqrt{B})\sqrt{T_2^\star}$. Consequently, the frequency-domain SNR and spin sensitivity become

$$\mathrm{SNR}_{f,i} = \frac{S_{\omega_{0,i}}}{2N_{rms}} = \frac{s_{0,i}\sqrt{T_2^\star}}{4\left(n_{rms}/\sqrt{B}\right)} \tag{3}$$

and

$$N_{min,f,i} \equiv \frac{N_i}{\mathrm{SNR}_{f,i}} = N_i \frac{2N_{rms}}{S_{\omega_{0,i}}} = \frac{4N_i\left(n_{rms}/\sqrt{B}\right)}{s_{0,i}\sqrt{T_2^\star}} = \alpha \frac{\left(4 n_{rms}/\sqrt{B}\right)}{\sqrt{T_2^\star}}, \tag{4}$$

respectively, where N_i is the number of spins in the sample contributing to the spectral component i and $\alpha = N_i/s_{0,i}$. For a detector with uniform unitary magnetic field B_u over the observable volume, we have $\alpha = 2B_u\omega_0^2\gamma^3\hbar^2 I(I+1)/(kT)$. The spin sensitivity is independent of the observed spectral line i, i.e. $N_{min,f} \equiv N_{min,f,i}$, but dependent on the $T_2^\star$ of the sample. In order to define a frequency-domain spin sensitivity independent of $T_2^\star$, i.e. independent of the B_0 inhomogeneity and the sample relaxation time T_2, we can introduce a normalized frequency-domain spin sensitivity defined as

$$\widetilde{N}_{min,f} \equiv \frac{N_i}{\mathrm{SNR}_{f,i}}\sqrt{\pi T_2^\star} = 4\alpha\sqrt{\pi}\left(n_{rms}/\sqrt{B}\right), \tag{5}$$

which corresponds to the spin sensitivity achievable for a $T_2^\star$ of $1/\pi$, i.e. a FWHM spectral line width of 1 Hz.

Alternatively, the spin sensitivity can also be defined in the time-domain according to

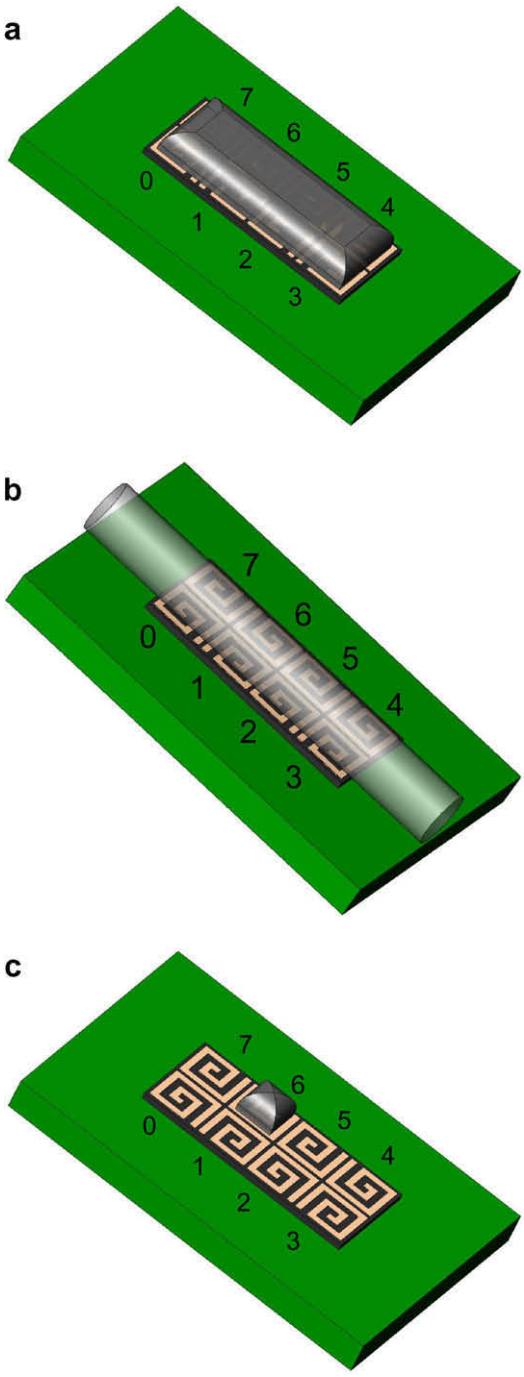

Fig. 9. Illustration of the different measurement setups. (a) PDMS sample over the entire array. (b) Capillary containing liquid sample over left half of the array. (c) PDMS sample over single channel.

$$N_{min,t} \equiv \frac{\sum_i N_i}{\mathrm{SNR}_t} = \frac{\sum_i N_i}{\sum_i s_{0,i} / \left[\left(n_{rms} / \sqrt{B} \right) \right]}. \quad (6)$$

The spin sensitivity in the time- and in the frequency-domain are then related in the following way:

$$\frac{\widetilde{N}_{min,f}}{N_{min,t}} = 4\sqrt{\pi}. \quad (7)$$

We have estimated the spin sensitivity of our integrated receiver using liquid (ethanol, toluene and water) as well as solid samples (PDMS) using different sample volumes and for different values of $T_2^{\star}$. For the frequency-domain spin sensitivity calculations a matched filter was applied.

The setup shown in Fig. 9c was used to estimate the spin sensitivity for a PDMS sample. Estimating the sample volume as $(500\ \mu\mathrm{m})^3$ and assuming a spin density of 4×10^{28} spins/m^3, we obtain a normalized frequency-domain spin sensitivity of 4×10^{15} spins/$\sqrt{\mathrm{Hz}}$.

The measurement results for a 12 nl and a 55 nl sample of water are displayed in Fig. 12. Assuming a spin density of 6.7×10^{28} spins/m^3, we obtain a normalized frequency-domain spin sensitivities of 4×10^{15} spins/$\sqrt{\mathrm{Hz}}$ and 5×10^{15} spins/$\sqrt{\mathrm{Hz}}$.

The spin sensitivity was also estimated using ethanol as sample. Using the 55 nl capillary mounted as shown in Fig. 9b and assuming a spin density of 6.1×10^{28} spins/m^3, we obtain a normalized frequency-domain spin sensitivity of 6×10^{15} spins/$\sqrt{\mathrm{Hz}}$.

As a final test, the spin sensitivity was evaluated using a toluene sample. Again, using the 55 nl capillary mounted as shown in Fig. 9b and assuming a spin density of 5.4×10^{28} spins/m^3, we obtain a normalized frequency-domain spin sensitivity of 6×10^{15} spins/$\sqrt{\mathrm{Hz}}$.

Table 2 summarizes the results of the spin sensitivity measurements. As expected, the obtained spin sensitivities are identical, within a factor of 2, for all samples.

The spin sensitivity achieved with a single channel of our integrated array is an order of magnitude worse than the best reported at any frequency (including 750 MHz measurements) [29–36]. However, the spin sensitivity in our approach can be significantly improved by the following three methods. A factor of $\sqrt{2}$ can be easily gained by using in-phase and quadrature (IQ) electronics for each channel. The use of thicker metal lines as they are available in the latest RF-CMOS technologies, some of which now offer two thick metal layers with thicknesses up to 4 μm in both copper and aluminum, will allow us to improve the intrinsic spin sensitivity by a factor of about $\sqrt{3}$. Finally, the spin sensitivity could be improved by increasing the bandwidth of the LNA to allow operation at higher frequencies. By going from 300 to 750 MHz we expect a gain of a factor 5. First post-layout simulations in a 0.13 μm technology show that the same receiver architecture and LNA topology can achieve bandwidths up to 900 MHz for a similar SNR performance by simple downscaling of the lengths of the input devices of the LNA. Therefore, an improvement larger than a factor of 10 is expected without any major changes in the methodology.

To evaluate the achievable spectral resolution of our chip, we used water samples with volumes of 12 and 55 nl, respectively. Using the conventional room temperature shimming coil system of our magnet, without any susceptibility matching material around the sensitive volume, we achieved a spectral resolution of about 4 Hz at FWHM and about 55 Hz at 5% of the peak amplitude, see Fig. 12. Although this spectral resolution is not sufficient for most spectroscopy applications, it will certainly be good enough for micro-imaging which is the main future application of out integrated micro-array.

3.3.2. Crosstalk experiment

As a last step to fully characterize the receiver array we analyzed the crosstalk between different channels. Although several papers already dealt with the issue of inter-channel crosstalk in NMR receiver arrays [7,37–39], we consider the problem from a slightly different perspective, which addresses the particular issues arising in densely packed integrated arrays.

We distinguish two major components of crosstalk: Electrical and physical crosstalk. Here, physical crosstalk refers to the induced voltage due to a sample placed on adjacent coils which results from the nonzero sensitivity, i.e. B_u-field, of one coil above neighboring channels. Electrical crosstalk, on the other hand, is due to the inductive and capacitive coupling between adjacent coils.

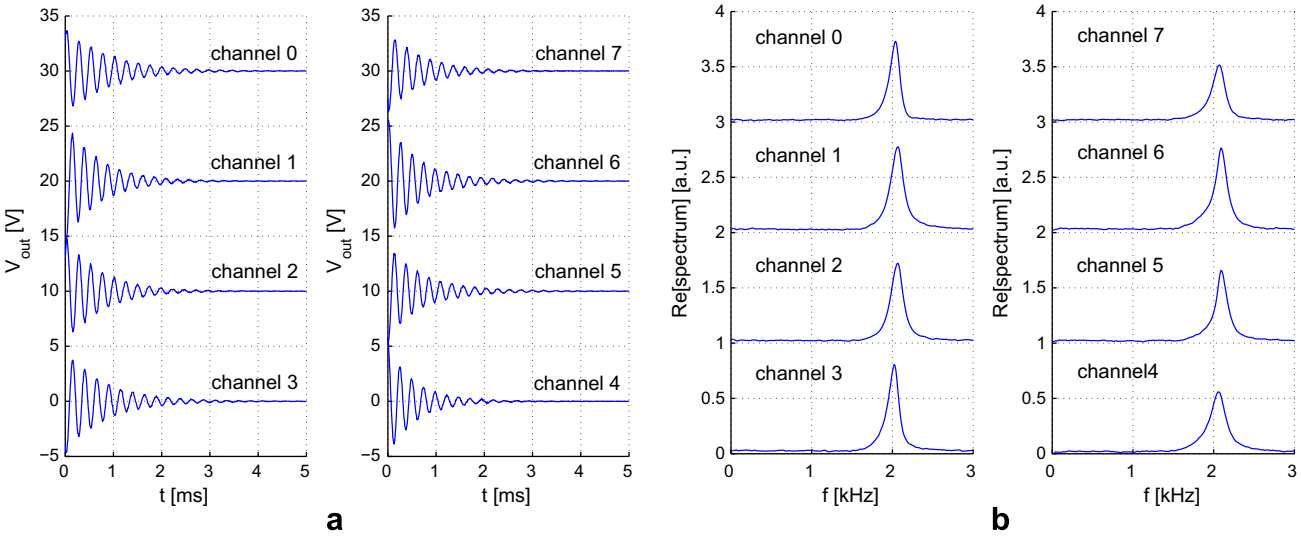

Fig. 10. Measurement results with a large PDMS sample covering the entire array. (a) Free-induction decay. (b) Real part of FFT.

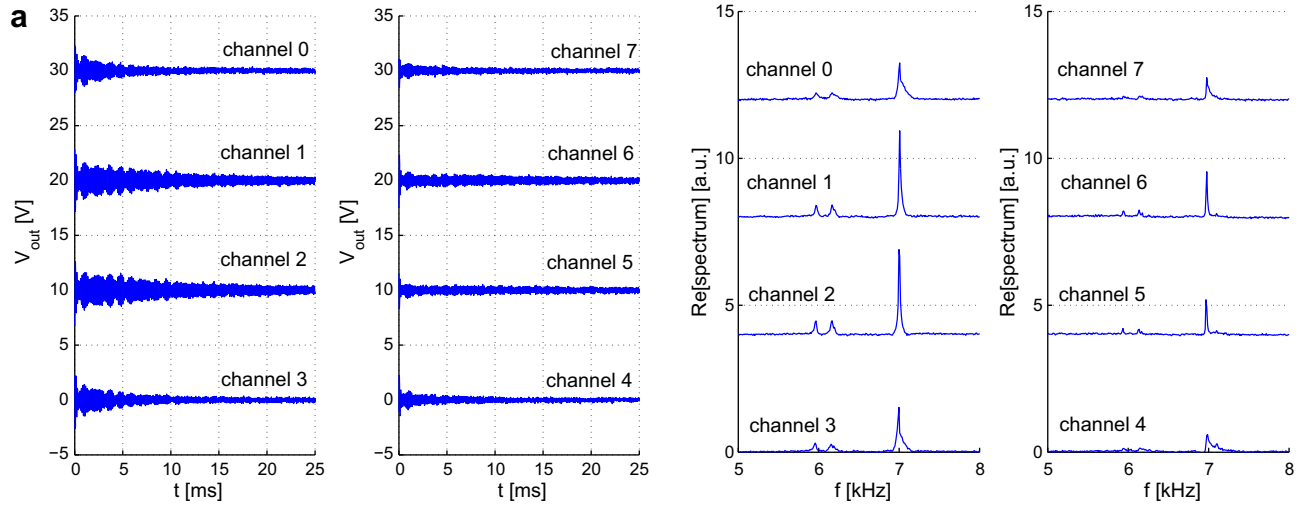

Fig. 11. Measurement results for an isopropanol sample covering channel 0–3. (a) Free-induction decay. (b) Real part of FFT.

We model the electrical crosstalk as primarily inductive in nature. Therefore, the electrical model of the reception array becomes the one shown in Fig. 13, where the mutual inductances M_{ij} represent the inductive coupling between channels, C_{tot} is the total capacitance in parallel to the reception coil, i.e. the parallel capacitor together with the equivalent parallel input capacitance of the LNA, L_{coil} is the coil self-inductance, R_{coil} is the effective coil resistance at 300 MHz and $\xi_{i,NMR}$ is the electro-motive force induced in the reception coil due to the sample. Due to the geometry of the array, i.e. the way the array was constructed by mirroring and shifting a copy of the same receiver cell, one has to pay special attention to the signs of the mutual inductances and the electromotive forces (emf's) in each channel.

The physical crosstalk is included in the model shown in Fig. 13 by calculating the voltage induced by the sample $\xi_{i,NMR}$ for each channel according to the reciprocity principle [26]

$$\xi_{i,NMR} = -\int_{V_s} \frac{d}{dt}\left(\vec{B}_{u,i}(\vec{r}) \cdot \vec{M}(t,\vec{r})\right) dV_s, \tag{8}$$

where $\vec{B}_{u,i}$ is the unitary magnetic field of reception coil i, $\vec{M}$ is the magnetization of the sample and V_s is the entire volume where $\vec{B}_{u,i} \cdot \vec{M} \neq 0$.

To estimate the relative contributions of physical and electrical crosstalk, we first consider a simplified model in which only two coils are present. A cubic sample of variable edge length is placed on one channel (channel 0) and the input voltage to the LNA of both channels, $v_{in,0}$ and $v_{in,1}$, is evaluated. The general solution to this problem can be obtained by solving the following system of linear equations

$$\begin{bmatrix} 0 \\ 0 \end{bmatrix} = \begin{bmatrix} Z & sM_{01} \\ sM_{10} & Z \end{bmatrix} \begin{bmatrix} i_0 \\ i_1 \end{bmatrix} + \begin{bmatrix} \xi_{0,NMR} \\ \xi_{1,NMR} \end{bmatrix}, \tag{9}$$

where s is the complex frequency variable and $Z = 1/(sC_{tot}) + R_{coil} + sL_{coil}$. The input voltages to the LNA's are then obtained by multiplying the resulting currents by $-1/(sC_{tot})$. To see the effect of the electrical crosstalk only, we have to set $\xi_{1,NMR}$ in Eq. (9) to zero and solve the resulting system to obtain the voltage at the LNA input due to electrical crosstalk only, $v_{in,1,electrical}$. If we set $\xi_{0,NMR}$ to zero, we obtain the input voltage due to physical coupling only (including a very small term due to the mutual inductance that is due to electrical crosstalk), $v_{in,1,physical}$. The results of these simulations are shown in Fig. 14. We see that the dominant source of coupling is clearly the electrical crosstalk. It is also

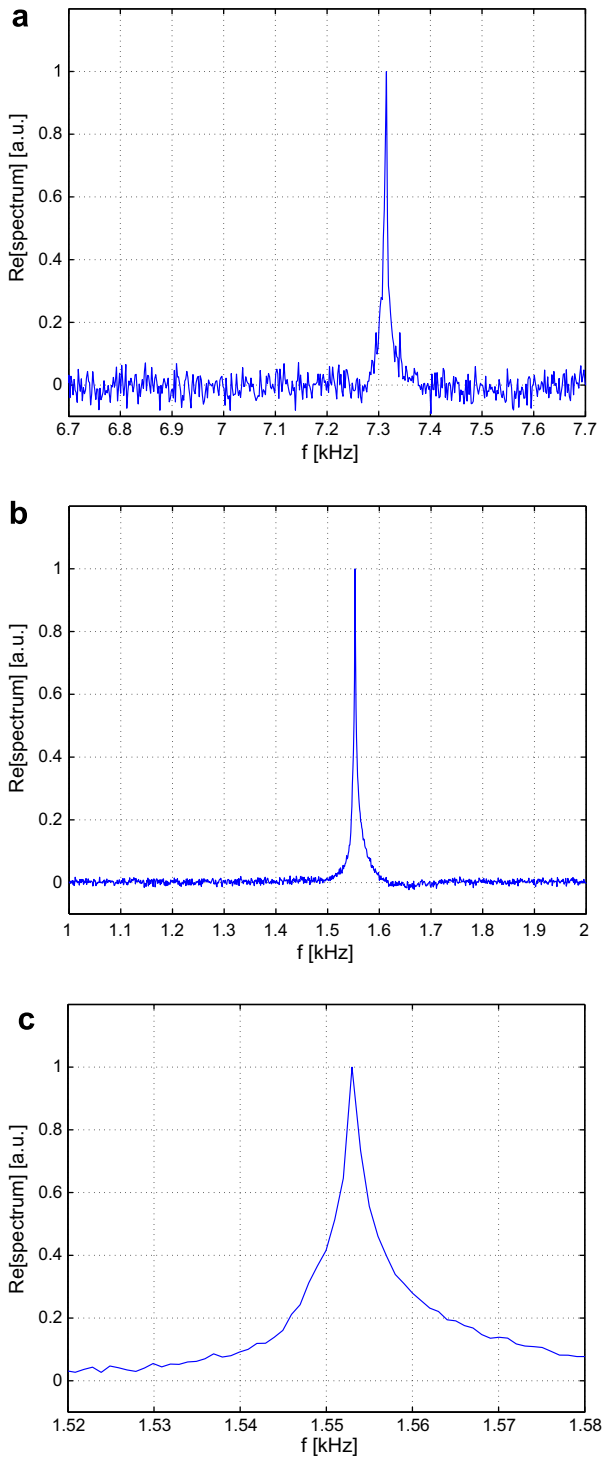

Fig. 12. Real part of FFT measured on a single channel, produced by a water sample covering channels 0 through 3. No filter applied. (a) Sample volume of 12 nl, T_{ACQ} = 0.5 s. (b) Sample volume of 55 nl, T_{ACQ} = 1 s. (c) Zoom-in of the spectral peak of the 55 nl sample to demonstrate the achievable linewidth.

interesting to see that, due to the coil orientations, the contributions of the electrical and the physical crosstalk have opposite polarity. Furthermore, the relative coupling is fairly constant for different sample sizes, possibly simplifying postprocessing algorithms.

In the first experiment, we used the excitation coil to homogeneously excite all channels of the array. In this experiment, because there is no sample placed, there is no physical crosstalk and therefore, we can measure the electrical crosstalk only. The relative signal amplitudes obtained in this experiment are shown in Table 3. It can be seen that the signals from all reception channels are within 12% of each other, with a maximum deviation from the predicted value of 15%.

For the second experiment, we placed a large, uniform PDMS-sample over the entire array. The measured output amplitudes for each channel are shown in the second column of Table 4. Again, we used the electrical coupling model to simulate the array's behavior. The maximum deviation between measurement and simulation is again below 15%.

As a last test, we placed a sample on only one channel and measured the output voltage on all array outputs. The data are shown in Table 5 together with the corresponding values obtained from a simulation using the electrical coupling model only. Also in this case, the maximum deviation between measurement and simulation is less than 20%.

The deviation between model and measurement can be attributed to the following factors. Firstly, the capacitive coupling between different coils is not reflected in the model. Secondly, there are effects from both the inhomogeneity of the excitation field, which was assumed to be constant over the receiver array, and the inhomogeneity of the sample, which was cut by hand and therefore will not be a perfect rectangular prism.

In summary, the main source of crosstalk is the electrical coupling due to the mutual inductance of the reception coils. Since the strength of the signal resulting from this undesired coupling can be as large as 20% of the original signal, one should take measures to cancel out these effects. The relatively good accuracy of the presented model suggests a straightforward way of calculating the induced voltages in each channel by simple digital postprocessing.

4. Conclusions and outlook

We present the first fully integrated reception array for NMR applications. The co-integration of the reception coil on the CMOS chip allows for a large number of coils in a densely packed array. The performance of the array was evaluated using electrical tests and NMR spectroscopy. We also characterized the crosstalk between different channels and gave models for both physical and electrical crosstalk. In the future, we will consider ways of reducing the electrical crosstalk by checking the integrability of the methods listed in [38] and further refine the model of the electrical crosstalk by incorporating some of the mutual capacitances between different coils. These efforts are necessary because mastering the crosstalk is certainly one of the main challenges in using the array for the target application of micro-MR imaging in a custom micro-gradient system specifically designed for micro-imaging using our single-chip integrated arrays. Furthermore, we are currently testing larger array sizes where the downconversion mixer and further baseband amplification stages are also integrated on the same chip. This should allow us to reduce the number of connections to the chip if proper multiplexing of the channels is applied on chip and thereby increase the number of possible channels in the array. Multiplexing at lower frequencies drastically relaxes the constraints on the associated multiplexers and cabling. The current trend in RF-CMOS technologies to increase the thickness of the top metal layer will allow us to progressively achieve better Q-factors with our integrated coils and thus to achieve better spin sensitivities. Another recent trend in modern RF-CMOS processes is to offer two thick top metal layers instead of only one. This option can be used to further boost the Q-factor by putting the two metal layers in parallel or to realize fully integrated phased-arrays [38].

Table 2
Summary of the time- and frequency-domain spin sensitivities obtained for different samples, different sample volumes and different values of $T_2^\star$, where $T_2^\star$ is the time constant for the optimal time-domain matched filter.

Sample	Vol. (nl)	$T_2^\star$ (ms)	$N_{min,t}$ (spins/$\sqrt{\text{Hz}}$)	$\tilde{N}_{min,f}$ (spins/$\sqrt{\text{Hz}}$)
PDMS	125	1	0.5×10^{15}	4×10^{15}
Water	12	30	0.8×10^{15}	4×10^{15}
	55	32	0.8×10^{15}	5×10^{15}
Ethanol	55	10	0.6×10^{15}	6×10^{15}
Toluene	55	15	0.9×10^{15}	6×10^{15}

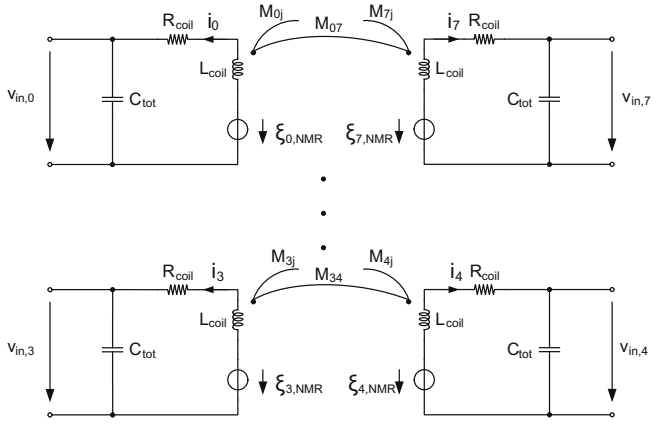

Fig. 13. Electrical crosstalk model of the reception array.

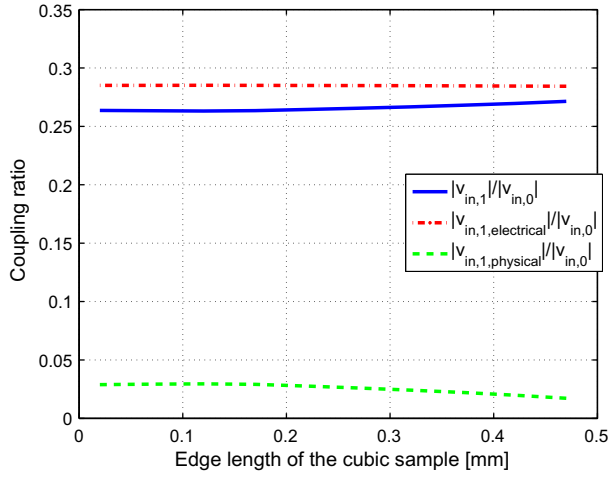

Fig. 14. Simulated coupling into adjacent channels split into contributions due to electrical crosstalk and physical crosstalk.

Table 3
Comparison between the measured, $v_{in,i,meas}$, and predicted, $v_{in,i,pred}$, voltages at the input of each amplifier, for a uniform B_1 excitation over the array. The predicted voltages are obtained by simulations from the model in Fig. 13. Values are normalized to channel 0.

Ch.	$v_{in,i,meas}$	$v_{in,i,pred}$	Dev. (%)
0 (Ref. ch.)	1	1	Ref.
1	1.12	1.07	5
2	1.12	1.08	4
3	1.08	1.04	4
4	1.06	1.05	1
5	1.08	1.18	9
6	1	1.18	15
7	0.96	1.09	12

Table 4
Comparison between the measured, $v_{in,i,meas}$, and predicted, $v_{in,i,pred}$, voltages at the input of each amplifier, with a PDMS sample covering the entire array (sample size: $\approx 3.5 \times 3.5 \times 1.5$ mm^3). The predicted voltages are obtained by simulations using the model shown in Fig. 13. Values are normalized to channel 0.

Ch.	$v_{in,i,meas}$	$v_{in,i,pred}$	Dev. (%)
0 (Ref. ch.)	1	1	Ref.
1	1.3	1.26	3
2	1.24	1.26	2
3	1.13	1.01	12
4	1.21	1.06	14
5	1.24	1.37	10
6	1.34	1.37	2
7	0.94	1.07	12

Table 5
Comparison between the measured, $v_{in,i,meas}$, and predicted, $v_{in,i,pred}$, voltages at each amplifier input, with a PDMS sample placed over channel 6 (sample size: $\approx 0.5 \times 0.5 \times 0.5$ mm^3). The predicted voltages are obtained by simulations using the model in Fig. 13. Values are normalized to channel 6.

Ch.	$v_{in,i,meas}$	$v_{in,i,pred}$	Dev. (%)
0	0.18	0.15	20
1	0.26	0.28	7
2	0.12	0.14	14
3	0.07	0.075	7
4	0.09	0.10	10
5	0.18	0.21	14
6 (Ref. ch.)	1	1	Ref.
7	0.24	0.25	4

Acknowledgment

This work is supported by the European Union under Contract No. 028533.

References

[1] C.J. Hardy, R.O. Giaquinto, J.E. Piel, K.W. Rohling, L. Marinelli, D.J. Blezek, E.W. Fiveland, R.D. Darrow, T.K.F. Foo, 128-Channel body MRI with a flexible high-density receiver-coil array, J. Magn. Reson. Imaging 28 (5) (2008) 1219–1225.
[2] M. Schmitt, A. Potthast, D.E. Sosnovik, J.R. Polimeni, G.C. Wiggins, C. Triantafyllou, L.L. Wald, A 128-channel receive-only cardiac coil for highly accelerated cardiac MRI at 3 tesla, Magn. Reson. Med. 59 (6) (2008) 1431–1439.
[3] C. Von Morze, J. Tropp, S. Banerjee, D. Xu, K. Karpodinis, L. Carvajal, C.P. Hess, P. Mukherjee, S. Majumdar, D.B. Vigneron, An eight-channel, nonoverlapping phased array coil with capacitive decoupling for parallel MRI at 3 t, Concepts Magn. Reson. B Magn. Reson. Eng. 31B (1) (2007) 37–43.
[4] U. Katscher, P. Bornert, Parallel magnetic resonance imaging, Neurotherapeutics 4 (3) (2007) 499–510.
[5] P. Vernickel, P. Roschmann, C. Findeklee, K.M. Ludeke, C. Leussler, J. Overwag, U. Katscher, I. Grasslin, K. Schunemann, Eight-channel transmit/receive body MRI coil at 3 t, Magn. Reson. Med. 58 (2) (2007) 381–389.
[6] H. Wang, Q. Xu, J.J. Ren, G.Y. Li, Four-channel magnetic resonance imaging receiver using frequency domain multiplexing, Rev. Sci. Instrum. 78 (1) (2007) 015102.
[7] M.A. Ohliger, D.K. Sodickson, An introduction to coil array design for parallel MRI, NMR Biomed. 19 (3) (2006) 300–315.

[8] H. Wang, L. Ciobanu, A.S. Edison, A.G. Webb, An eight-coil high-frequency probehead design for high-throughput nuclear magnetic resonance spectroscopy, J. Magn. Reson. 170 (2) (2004) 206–212.
[9] T. Hou, J. Smith, E. MacNamara, M. Macnaughtan, D. Raftery, Analysis of multiple samples using multiplex sample NMR: selective excitation and chemical shift imaging approaches, Anal. Chem. 73 (11) (2001) 2541–2546.
[10] Y. Li, A.M. Wolters, P.V. Malawey, J.V. Sweedler, A.G. Webb, Multiple solenoidal microcoil probes for high-sensitivity, high-throughput nuclear magnetic resonance spectroscopy, Anal. Chem. 71 (21) (1999) 4815–4820.
[11] E. MacNamara, T. Hou, G. Fisher, S. Williams, D. Raftery, Multiplex sample NMR: an approach to high-throughput NMR using a parallel coil probe, Anal. Chim. Acta 397 (1-3) (1999) 9–16.
[12] M.A. Macnaughtan, T. Hou, J. Xu, D. Raftery, High-throughput nuclear magnetic resonance analysis using a multiple coil flow probe, Anal. Chem. 75 (19) (2003) 5116–5123.
[13] D. Raftery, High-throughput NMR spectroscopy, Anal. Bioanal. Chem. 378 (6) (2004) 1403–1404.
[14] J.R. Spadea, S.M. Wright, Optimization of printed coil arrays for microscopic imaging and spectroscopy, in: Proceedings of the 19th Annual International Conference of the Ieee Engineering in Medicine and Biology Society, vol. 19, pts. 1–6 19, 1997, pp. 464–466.
[15] H. Wang, L. Ciobanu, A. Webb, Reduced data acquisition time in multi-dimensional NMR spectroscopy using multiple-coil probes, J. Magn. Reson. 173 (1) (2005) 134–139.
[16] H. Lee, E. Sun, D. Ham, R. Weissleder, Chip-NMR biosensor for detection and molecular analysis of cells, Nat. Med. 14 (8) (2008) 869–874.
[17] D.L. Olson, T.L. Peck, A.G. Webb, R.L. Magin, J.V. Sweedler, High-resolution microcoil H-1-NMR for mass-limited, nanoliter-volume samples, Science 270 (5244) (1995) 1967–1970.
[18] A.G. Webb, Radiofrequency microcoils in magnetic resonance, Progr. Nucl. Magn. Reson. Spectrosc. 31 (1997) 1–42.
[19] A. Purea, T. Neuberger, A.G. Webb, Simultaneous NMR microimaging of multiple single-cell samples, Concepts Magn. Reson. B Magn. Reson. Eng. 22B (1) (2004) 7–14.
[20] T. Wang, L. Ciobanu, X.Z. Zhang, A. Webb, Inductively coupled RF coil design for simultaneous microimaging of multiple samples, Concepts Magn. Reson. B Magn. Reson. Eng. 33B (4) (2008) 236–243.
[21] G. Boero, J. Frounchi, B. Furrer, P.A. Besse, R.S. Popovic, Fully integrated probe for proton nuclear magnetic resonance magnetometry, Rev. Sci. Instrum. 72 (6) (2001) 2764–2768.
[22] G. Boero, C. de Raad Iseli, P.A. Besse, R.S. Popovic, An NMR magnetometer with planar microcoils and integrated electronics for signal detection and amplification, Sensors Actuators A Phys. 67 (1–3) (1998) 18–23.
[23] T. Cherifi, N. Abouchi, G.N. Lu, L. Bouchet-Fakri, L. Quiquerez, B. Sorli, J.F. Chateaux, M. Pitaval, P. Morin, A CMOS microcoil-associated preamplifier for NMR spectroscopy, IEEE Trans. Circ. Syst. I Regul. Pap. 52 (12) (2005) 2576–2583.
[24] A. Hassibi, A. Babakhani, A. Hajimiri, A spectral-scanning magnetic resonance imaging (MRI) integrated system, in: Custom Integrated Circuits Conference, 2007, CICC '07, IEEE, 2007, pp. 123–126, doi:10.1109/CICC.2007.4405695.
[25] Y. Liu, N. Sun, H. Lee, R. Weissleder, D. Ham, CMOS mini nuclear magnetic resonance system and its application for biomolecular sensing, in: Solid-State Circuits Conference, 2008, ISSCC 2008, Digest of Technical Papers, IEEE International, 2008, pp. 140–602, doi:10.1109/ISSCC.2008.4523096.
[26] D.I. Hoult, The principle of reciprocity in signal strength calculations – a mathematical guide, Concepts Magn. Reson. 12 (4) (2000) 173–187.
[27] J. Anders, G. Boero, A low-noise CMOS receiver frontend for MRI, in: Biomedical Circuits and Systems Conference, 2008, BioCAS 2008, IEEE, 2008, pp. 165–168.
[28] W.M.C. Sansen, Analog Design Essentials, Springer, 2006.
[29] D.L. Olson, J.A. Norcross, M. O'Neil-Johnson, P.F. Molitor, D.J. Detlefsen, A.G. Wilson, T.L. Peck, Microflow NMR: concepts and capabilities, Anal. Chem. 76 (10) (2004) 2966–2974.
[30] K. Ehrmann, N. Saillen, F. Vincent, M. Stettler, M. Jordan, F.M. Wurm, P.A. Besse, R. Popovic, Microfabricated solenoids and helmholtz coils for NMR spectroscopy of mammalian cells, Lab Chip 7 (3) (2007) 373–380.
[31] S. Leidich, M. Braun, T. Gessner, T. Riemer, Silicon cylinder spiral coil for nuclear magnetic resonance spectroscopy of nanoliter samples, Concepts Magn. Reson. B Magn. Reson. Eng. 35B (1) (2009) 11–22.
[32] Y. Maguire, I.L. Chuang, S.G. Zhang, N. Gershenfeld, Ultra-small-sample molecular structure detection using microslot waveguide nuclear spin resonance, Proc. Natl. Acad. Sci. USA 104 (22) (2007) 9198–9203.
[33] P.J.M. van Bentum, J.W.G. Janssen, A.P.M. Kentgens, J. Bart, J.G.E. Gardeniers, Stripline probes for nuclear magnetic resonance, J. Magn. Reson. 189 (1) (2007) 104–113.
[34] A.P.M. Kentgens, J. Bart, P.J.M. van Bentum, A. Brinkmann, E.R.H. Van Eck, J.G.E. Gardeniers, J.W.G. Janssen, P. Knijn, S. Vasa, M.H.W. Verkuijlen, High-resolution liquid- and solid-state nuclear magnetic resonance of nanoliter sample volumes using microcoil detectors, J. Chem. Phys. 128 (5) (2008).
[35] C. Massin, F. Vincent, A. Homsy, K. Ehrmann, G. Boero, P.A. Besse, A. Daridon, E. Verpoorte, N.F. de Rooij, R.S. Popovic, Planar microcoil-based microfluidic NMR probes, J. Magn. Reson. 164 (2) (2003) 242–255.
[36] M.E. Lacey, R. Subramanian, D.L. Olson, A.G. Webb, J.V. Sweedler, High-resolution NMR spectroscopy of sample volumes from 1 nl to 10 μl, Chem. Rev. 99 (10) (1999) 3133.
[37] R.F. Lee, R.O. Giaquinto, C.J. Hardy, Coupling and decoupling theory and its application to the MRI phased array, Magn. Reson. Med. 48 (1) (2002) 203–213.
[38] S.M. Wright, L.L. Wald, Theory and application of array coils in mr spectroscopy, NMR Biomed. 10 (8) (1997) 394–410.
[39] G.R. Duensing, H.R. Brooker, J.R. Fitzsimmons, Maximizing signal-to-noise ratio in the presence of coil coupling, J. Magn. Reson. Ser. B 111 (3) (1996) 230–235.